Medical Physics
The International Journal of Medical Physics Research and Practice

Inter-slice bidirectional registration-based segmentation of the prostate gland in MR and CT image sequences

Farzad Khalvati, Aryan Salmanpour, Shahryar Rahnamayan, George Rodrigues, and Hamid R. Tizhoosh

Citation: Medical Physics **40**, 123503 (2013); doi: 10.1118/1.4829511
View online: http://dx.doi.org/10.1118/1.4829511
View Table of Contents: http://scitation.aip.org/content/aapm/journal/medphys/40/12?ver=pdfcov
Published by the American Association of Physicists in Medicine

Inter-slice bidirectional registration-based segmentation of the prostate gland in MR and CT image sequences

Farzad Khalvati[a)]
Department of Systems Design Engineering, University of Waterloo, Waterloo, Ontario N2L 3G1, Canada

Aryan Salmanpour and Shahryar Rahnamayan
Department of Engineering and Applied Science, University of Ontario Institute of Technology, Oshawa, Ontario L1H 7K4, Canada

George Rodrigues
Department of Radiation Oncology, London Regional Cancer Program, London, Ontario N6C 2R6, Canada and Department of Epidemiology/Biostatistics, University of Western Ontario, London, Ontario N6A 3K7, Canada

Hamid R. Tizhoosh
Department of Systems Design Engineering, University of Waterloo, Waterloo, Ontario N2L 3G1, Canada

(Received 19 June 2013; revised 21 October 2013; accepted for publication 22 October 2013; published 13 November 2013)

Purpose: Accurate segmentation and volume estimation of the prostate gland in magnetic resonance (MR) and computed tomography (CT) images are necessary steps in diagnosis, treatment, and monitoring of prostate cancer. This paper presents an algorithm for the prostate gland volume estimation based on the semiautomated segmentation of individual slices in T2-weighted MR and CT image sequences.
Methods: The proposed *Inter-Slice Bidirectional Registration-based Segmentation* (iBRS) algorithm relies on interslice image registration of volume data to segment the prostate gland without the use of an anatomical atlas. It requires the user to mark only three slices in a given volume dataset, i.e., the first, middle, and last slices. Next, the proposed algorithm uses a registration algorithm to autosegment the remaining slices. We conducted comprehensive experiments to measure the performance of the proposed algorithm using three registration methods (i.e., rigid, affine, and nonrigid techniques).
Results: The results with the proposed technique were compared with manual marking using prostate MR and CT images from 117 patients. Manual marking was performed by an expert user for all 117 patients. The median accuracies for individual slices measured using the Dice similarity coefficient (DSC) were 92% and 91% for MR and CT images, respectively. The iBRS algorithm was also evaluated regarding user variability, which confirmed that the algorithm was robust to interuser variability when marking the prostate gland.
Conclusions: The proposed algorithm exploits the interslice data redundancy of the images in a volume dataset of MR and CT images and eliminates the need for an atlas, minimizing the computational cost while producing highly accurate results which are robust to interuser variability. [http://dx.doi.org/10.1118/1.4829511]

Key words: image registration, prostate segmentation, magnetic resonance imaging, computed tomography imaging, prostate volume

1. INTRODUCTION

Prostate cancer is the most common cancer in men. For example, one in six men in Canada is diagnosed with prostate cancer during their lifetime.[1] However, it is a slow-growing type of cancer and, in most cases, its diagnosis usually leads to active monitoring of tumor growth for a long period of time. An important part of monitoring prostate cancer is prostate gland volume estimation, which plays a significant role in deciding the next step, i.e., active surveillance, surgery/radiation treatment, or an assessment of the applicability or safety of brachytherapy (i.e., large prostate glands can be difficult or impossible to implant, which leads to increased toxicity). Currently, CT images are generally used for radiation therapy planning because density information is essential for accurately calculating the beam intensities. In many cases, however, MR images are also used for accurate image segmentation because, from the expert user's perspective, MR images contain detailed information of the organs and/or tumors under study. In such cases, it is generally necessary to register MR images with CT scans to produce the markings required for planning.

Recent research has delivered promising results where MR images can be used as an alternative to the more widely used CT scans. MR imaging is a safer and less invasive method compared with CT scans. The use of MRI could also potentially reduce inter-observer variability. Even in cases where the treatment planning has been decided, MR imaging has begun to gain momentum because of its soft-tissue contrast and high spatial resolution.[2–4] Recent studies show that MR

images can be used for dose calculation in cancer treatment, which might lead to the complete elimination of the requirement for CT.[5] In all cases of diagnosis, treatment, and monitoring of prostate cancer, accurate localization and segmentation of the prostate gland in images is required.

MR (or CT) volume datasets ("Volume dataset" refers to image sequences of a volumetric object such as a prostate gland, which are captured during a single scan.) are captured to estimate the volume of the prostate gland. Each slice of the volume dataset has to be marked (We refer to the manual and automatic marking of an object in images as "contouring" and "autosegmenting/segmenting", respectively.) so the boundary of the prostate gland can be labeled. Currently, this is performed manually by clinical experts (e.g., radiologists and oncologists) and contouring of a patient's volume dataset can take several minutes. For example, manual contouring of the prostate in a MR image series containing 15 slices could take around 15 min, depending on the expertise and working speed of the clinician. Given a large number of prostate cancer cases (considering the effect of an aging population), the long time required to process the volume dataset imposes a serious burden on the healthcare system and prevents timely patient access to proper care. The availability of a computer-assisted segmentation method could reduce the time spent manually contouring the prostate during this high-demand everyday task in hospitals.

Atlas-based segmentation (ABS) is a well-established and widely used technique for extracting contours from medical images. In this method, the processed images are stored in a database known as an atlas, along with their optimal segmentation results. A target image is usually registered and compared with the atlas, and the result of the best match is selected as the segmentation result, which is then deformed using the registration transformation. Proposed ABS methods have been partially successful at segmenting medical images, but they have major shortcomings that limit the efficiency of the technique. First, the accuracy of the results depends on the diversity of the atlas or the atlas selection. It is virtually impossible to produce an atlas that is sufficiently diverse by careful atlas selection so it will provide good results for all unseen images. Therefore, a practical solution is to make the atlas as large as possible so there is a higher chance that the target image matches one in the atlas. However, even large atlases cannot guarantee a reasonable result for any target image. It is always possible that the target image will not match any image in the atlas, which leads to poor results. Second, ABS algorithms are based on multiple image registrations. Image registration is a computationally demanding algorithm and the ABS requirement for multiple registrations makes it computationally expensive. Third, an atlas created from the images of a particular scanner can usually only be used to segment images from the same scanner due to the fact that different scanners produce images with different characteristics. This is yet another limitation for ABS algorithms where the atlas and target images must be of the same scanner and/or imaging protocol in order to achieve highly accurate results.

The aim of the current study was to develop an algorithm that exploits interslice redundancy to segment the prostate gland in MR and CT images without any need for an atlas. Our algorithm benefits from the interslice data redundancy of images in a volume dataset so a given label (We refer to the result of contouring or autosegmentation of an image as a "label".) can be propagated to the neighboring slices using image registration. This eliminates the need for an atlas, which removes the burden of creating an appropriate atlas.

We evaluated the performance of our proposed algorithm using the volume datasets from 100 patients MR images ("One patient image" refers to a volume dataset captured during a single scan.) and 17 volume datasets of CT images, which were manually contoured by an expert user. A comparison of the unedited segmentation results using our algorithm with manually contoured images demonstrated their high accuracy for volume estimation and the marking of individual slices of prostate gland in MR and CT images. The fact that the iBRS algorithm produced highly accurate results for both MR and CT images indicate that our proposed algorithm is modality independent, so it is applicable to MR and CT. We also evaluated the robustness of our proposed algorithm with regard to user variability in contouring MR images by comparing the performance of the algorithm with contouring by five different expert users with the volume datasets for 15 patients (different than the original MRI data from 100 patients).

The outline of the remainder of this paper is as follows. In Sec. 2, the related work on the segmentation of prostate images is presented. Section 3 presents a brief background review of different image registration techniques. In Sec. 4, we present our proposed algorithm for semiautomatic segmentation of prostate gland in MR and CT images. Sections 5 and 6 present the performance results and the discussion for the proposed algorithm, respectively. Finally, Sec. 7 concludes the paper.

2. RELATED WORK

Several methods, which are based on manually contoured images and estimated measurements of the prostate, have been proposed for estimating the prostate volume by modeling the prostate as a simple geometric shape. The ellipsoid model is one of the most popular models for estimating the prostate volume.[6–8] The main drawback of the ellipsoid model is that it sometimes underestimates the prostate volume.[8]

Active shape models (ASMs) have been proposed for the automatic segmentation and recognition of biomedical organs.[9] The general concept of ASMs is that a shape model is constructed based on the principal component analysis (PCA) of several landmark points, which are determined manually using a set of training images.[10] ASMs have been widely used for the segmentation of prostate glands, mostly in ultrasound images.[11–14] Recently, Toth *et al.*[15] proposed a method for estimating the prostate volume in MR images using ASMs. Their method involved training an ASM with a set of training images based on multiple features. They also compared their results with other models and showed that their method performed better than the ellipsoid model when estimating the prostate volume.

Another popular approach for prostate segmentation is atlas-based segmentation (ABS).[16–20] Briefly, this method involves contouring the desired anatomy (i.e., prostate) by an expert user and storing the original images with the corresponding labels (i.e., segmented binary image) in a database known as an "atlas." To segment the prostate in a target image, all of the images in the atlas are registered to the target image using an image registration method. The registered images in the atlas are then compared to the target image using an image similarity matching technique to find the most similar registered image in the atlas. Finally, a segmented image is produced by applying an image transformation function to the segmented binary image (label) that corresponds to the most similar image in the atlas. Among the prostate registration algorithms in the literature, the ABS methods are the most relevant methods to our proposed iBRS algorithm because both methods heavily rely on image registration. Therefore, as related work, we focus on ABS algorithms for which different variations have been proposed to increase the accuracy of the results and/or reduce the computational cost.

Klein *et al.*[18] presented a semiautomatic algorithm based on atlas matching for the segmentation of the prostate gland in MR images. The algorithm used an affine registration followed by a nonrigid registration method to register all of the images in the atlas with the target image. The registered images were compared to the target image using mutual information as the similarity measure to select a set of the most similar registered images. For each selected registered image, the corresponding image transformation was applied to the original segmented image (or label) to produce the registered label. The generated labels were then averaged together and thresholded at 50% to generate the final label. The regions of interest (ROIs) that needed to be segmented in the atlas and the images were selected manually. The atlas and test data comprised 14 and 22 images, respectively. A median Dice similarity coefficient (DSC) of 82% was reported but the processing time was not mentioned.

In another study, Klein *et al.*[17] presented an improved version of their previous method.[18] The first stage of this algorithm (atlas selection) was similar to the previous method[18] which produced a set of registered labels. The registered labels were then fused using two methods: majority voting and simultaneous truth and performance level estimation (STAPLE).[21] The registered labels were fed to these two methods to generate a consensus label. Next, the registered labels were compared with the consensus and the least similar labels were discarded, whereas the remainder were used to create a new consensus label. This process required several iterations until the remaining labels were similar to their consensus labels. The final consensus label was considered to be the final result for a given image. The ROIs that needed to be segmented in the atlas and the images were selected manually. Two experiments were conducted. The atlas and test data used in experiments 1 and 2 comprised 38 and 50 scans, and 50 and 50 scans, respectively. Using the best settings for the atlas selection, similarity measure, and label fusion, a median DSC of 88% was reported. The processing time per registration was 15 min on a single Pentium 2.4 GHz processor.

Dowling *et al.*[19] proposed a segmentation method based on probabilistic atlases that used a nonrigid registration method. In this method, a volume dataset (scan) was selected as the initial atlas. The remaining volume datasets with labels were registered twice against the initial atlas. First, using rigid and affine transformations and then using rigid, affine, and nonrigid transformations. A new atlas was generated at the end of each step by averaging the registered images. The registered labels were also averaged to produce a probability map of the prostate. To segment a target image, the average atlas was registered against it using affine and nonrigid registration methods. The transformation was then applied to the probability map of the prostate and the result was thresholded to generate the result label. The atlas and test data for the experiments comprised 15 and one scans, respectively. A median DSC of 78% was reported for the cases that did not fail completely. The processing time was 60 min for the test scan on a dual core Intel 3 GHz processor.

Langerak *et al.*[20] proposed a multiatlas-based segmentation method for prostate MR images based on an iterative label fusion approach, which was somewhat similar to the algorithm proposed in Ref. 17. First, all of the atlas images were registered (affine followed by nonrigid) against the target image to obtain a set of registered labels. The segmentation performance was estimated based on normalized mutual information and the registered labels were then fused together using a weighted majority voting method. Next, the overlap of each contour was calculated against the fused label. Labels with low overlaps were dropped and the fused labels were recalculated. The atlas and test data used in the experiments both comprised 99 images. An average DSC of 87.5% was reported. The processing time was 8 min and 23 s per image for postregistration only on a 2.66 GHz dual processor.

Martin *et al.*[16] proposed a probabilistic atlas-based segmentation method for prostate MR images. The atlas was created by registering (affine followed by nonrigid) images with a manually picked reference image. Next, a mean image was created by averaging all of the registered images. Each image was registered against the mean image to produce a deformed label of the image. The deformed labels were then averaged to generate a probability map of the labels. To segment an image, the mean image was registered to it and the probability map of the labels was deformed using the registration transform. The result label was modified using a deformable model to better match the prostate boundaries. The atlas and test data used in the experiments both comprised 36 scans. A median DSC of 87% was reported. The processing time was 4 min on a dual core 1.6 GHz processor because the algorithm only required one registration per image.

The proposed atlas-based segmentation techniques all provide reasonable results (DSCs of up to 88%). A drawback is the atlas generation process where a clinician (e.g., a radiation oncologist) must contour several images manually to create a database of images and their corresponding labels. This is a time-consuming task and it might not always be possible to have a preprocessed dataset. A second drawback is the computational time required to process the proposed algorithms. In most cases, the algorithm requires that all images in the

atlas must be registered against the target image. Registration is an intensive task and registering multiple images is prohibitively expensive (e.g., 15 min per registration in Ref. 17). The algorithm proposed in Ref. 16 reduced the computational time drastically by creating a mean image that was used to register the target image, but it still required postprocessing to deform the registered label appropriately. The reported time was significantly less than the other proposed algorithms (i.e., 4 min).

Instead of using a pregenerated atlas, our proposed algorithm uses the three initial labels generated by the user before producing the labels of the remaining images in the volume dataset. Our results show that using expert knowledge to initialize three labels (apex, base, and middle slice) leads to a high accuracy (above 88% DSC) without using an atlas and in a much shorter time (i.e., 13 s per volume dataset) compared with previously proposed algorithms.

It should be mentioned that the idea of propagating a preprocessed label through the slices of 3D images of prostate has been utilized in the literature to segment TRUS prostate (transrectal ultrasound) images. A semiautomatic segmentation algorithm was proposed in Ref. 22 where the user initializes the algorithm by clicking on six points of the prostate boundary in the midgland. The image is then unwarped to reduce the deformation effect of the TRUS probe. An ellipse is then fitted to the midgland to obtain its parameters. The fitted ellipsoid is used to guide an edge detection algorithm to obtain the final contour for the midgland. The contour is then propagated to the remaining slices to be used as initial points for fitting. The result accuracy in terms of volume ratio was 93%. Qiu *et al.*[23] proposed a semiautomated method in which the user initializes the algorithm by selecting points on the boundary of prostate in the first slice. The algorithm then uses a level set function to extract the contour for the first slice which is then propagated to the next slice as the initial contour and shape constraint for segmentation using the level set function. The proposed algorithm was applied to 3D TRUS images of 30 patients where an average DSC of 93% was achieved. The processing time for the segmentation run on dual core Intel 2.66 GHz was 55 s.

In contrast to our proposed algorithm, these algorithms do not use registration to propagate a contour from one slice to the next. Instead, they use the initial contour as the shape constraint or initial points for the segmentation algorithm (e.g., level set or edge detector) applied to the remaining slices.

3. IMAGE REGISTRATION: BACKGROUND REVIEW

Image registration is the underlying basis of the iBRS algorithm proposed in this paper, so we briefly review the three main image registration techniques used by our proposed algorithm. Comprehensive surveys of image registration methods have been provided by Refs. 24 and 25.

The first registration method is rigid registration, which facilitates the scaling, rotation, and translation of the source image. Rigid transformation can be written in 2D homogeneous coordinates as

$$p_2 = \mathrm{SRT}\, p_1, \tag{1}$$

where $p_1 = [x_1 \quad y_1 \quad 1]^T$ and $p_2 = [x_2 \quad y_2 \quad 1]^T$. S, T, and R represent the scaling, translation, and rotation matrices, respectively, as follows:

$$S = \begin{bmatrix} s_x & 0 & 0 \\ 0 & s_y & 0 \\ 0 & 0 & 1 \end{bmatrix}, T = \begin{bmatrix} 1 & 0 & t_x \\ 0 & 1 & t_y \\ 0 & 0 & 1 \end{bmatrix}, \tag{2}$$

$$R = \begin{bmatrix} \cos(\theta) & -\sin(\theta) & 0 \\ \sin(\theta) & \cos(\theta) & 0 \\ 0 & 0 & 1 \end{bmatrix}. \tag{3}$$

The second image registration method used by the proposed algorithm is affine registration, which is a more general form of rigid registration. In addition to scaling, translation, and rotation, this allows the shearing of the source image. The affine transformation matrix can be written as follows:

$$A = \begin{bmatrix} a_{11} & a_{12} & t_x \\ a_{21} & a_{22} & t_y \\ 0 & 0 & 1 \end{bmatrix}. \tag{4}$$

Six parameters need to be optimized for the affine transformation without any restrictions on the elements a_{ij}. In our experiments, an open source implementation[26] was used for both rigid and affine registration methods in which sum of squared differences (SSD) was used as the similarity measure (cost function) for the registration

$$\mathrm{SSD} = \frac{1}{n}\sum_{i=1}^{n}(M(i) - F(i))^2, \tag{5}$$

where F and M are static and moving images, respectively, and n is the number of pixels in each image.

The third registration method used in this paper is a nonrigid registration technique known as the Demon algorithm.[27] The Demon method is a well-known nonrigid registration algorithm that has been successfully used in registering medical images in different modalities.[28,29] It employs the concept of an optical flow equation to find small deformations in temporal image sequences. Let F and M be static and moving images, respectively, and f and m be the intensities of the static and moving images, respectively. For a given point p in the static image, the estimated displacement (i.e., velocity) $\mathbf{u}$ required for point p to match the corresponding point in M is given by[27]

$$\mathbf{u} = \frac{(m - f)\nabla f}{|\nabla f|^2 + (m - f)^2}, \tag{6}$$

where $\mathbf{u} = (u_x, u_y)$ in 2D, and ∇f is the gradient of the static image. The term $(m - f)^2$ was added by Thirion[27] to stabilize the velocity equation so it can be used for image registration. The velocity $\mathbf{u}$ is based on local information in the static and moving images. Therefore, Gaussian smoothing (G_{Fluid}) of the velocity field is usually included as a regularization method for image registration purposes. The original equation [Eq. (6)] uses the edge information only from the fixed image. Wang *et al.*[28] modified the equation to also include the edge information from the moving image. The Demon equation is

solved iteratively to register two images as follows:

$$\mathbf{u}^N = G_{\text{Fluid}} * \mathbf{u}^{N-1} + \frac{(m^{N-1} - f)\nabla f}{|\nabla f|^2 + \alpha^2(m^{N-1} - f)^2} + \frac{(m^{N-1} - f)\nabla m}{|\nabla m|^2 + \alpha^2(m^{N-1} - f)^2}, \quad (7)$$

where α is a normalization factor[30] and m^{N-1} is a transformed version of the moving image calculated using $\mathbf{u}$ at stage $N-1$. m^{N-1} can be written as $G_{\text{Diff}} * T^{N-1}(m^{N-2})$ where T is the transformation field smoothed by a Gaussian filter G_{Diff}.

In our experiments, an open source implementation[26] was used for Demon registration algorithm for which, the following parameters were used:

- $\sigma_{\text{Fluid}} = 4$: the standard deviation for the Gaussian smoothing kernel (G_{Fluid}) of the pixel velocity field.
- $\sigma_{\text{Diff}} = 1$: the standard deviation for the Gaussian smoothing kernel (G_{Diff}) of the transformation field.
- Interpolation: Linear.
- $\alpha = 4$: a constant that reduces the effects of edges and noise.

4. PROPOSED ALGORITHM

The contouring of medical images for prostate is usually performed for prostate cancer detection[31] and treatment planning for radiation therapy.[32] In prostate cancer detection which usually includes active surveillance (or monitoring the disease), one of the important tasks is to estimate the volume of the prostate in order to calculate the PSA (Prostate-Specific Antigen) density. The PSA density can be sensitive to changes in the volume, particularly in low PSA situations (as found during screening). The iBRS was designed with this specific clinical workflow in mind. The clinician is only required to contour three slices of the volume dataset and the algorithm autogenerates the labels for the remaining slices. The accuracy of the estimated volume or volume ratio is usually sufficiently high (90% and 1.11, respectively) for active surveillance purposes.

Images in a volume dataset share a large amount of information, especially those that are consequent to each other, because they represent different crosssections of the same volumetric object. In this scenario, image registration should yield a better result without any need for a large atlas of images. This is the underlying concept of the iBRS algorithm proposed in this paper. The proposed algorithm registers images in a given volume dataset against each other, thereby eliminating the need to create an atlas. It can use rigid, affine, or nonrigid registration methods to generate labels.

The iBRS algorithm automatically generates labels for the individual slices in a given volume dataset of prostate gland MR/CT images, provided that the user contours the prostate gland in the first, middle, and last slice of the volume. We consider a set of $n+1$ slices of prostate gland in a MR/CT sequence $\{I_k\}_{k=0,\ldots,n}$ with the slice thickness Th. The iBRS algorithm can be summarized as follows:

(1) *Initialization:* An expert user contours the prostate in three slices I_0, $I_{\lfloor \frac{n}{2} \rfloor}$, and I_n, which are the first (i.e., base), middle (i.e., midgland), and last (i.e., apex) slices in the image sequence. This produces the labels for the three slices: L_0, $L_{\lfloor \frac{n}{2} \rfloor}$, and L_n. Three ROIs are built around the user's labels. A linear interpolation algorithm is used to calculate the interpolated ROIs for the remaining slices in the image sequence (i.e., between I_0 and $I_{\lfloor \frac{n}{2} \rfloor}$, and between $I_{\lfloor \frac{n}{2} \rfloor}$ and I_n). The largest ROI of the two is used when registering one slice with the other.

(2) *Image registration direction 1:*

- Starting from I_0 and moving forward toward $I_{\lfloor \frac{n}{2} \rfloor - 1}$, each image is registered to the next image as follows:

$$T_{i-1}^{r_1} = Reg(I_{i-1}, I_i), \quad (8)$$

where *Reg* is a registration method (rigid, affine, or nonrigid) and $i \in \{1, \ldots, \lfloor \frac{n}{2} \rfloor - 1\}$. At each step i, the computed registration transformation, $T_{i-1}^{r_1}$, is applied to slice I_{i-1} and its label, L_{i-1}, which generates the registered image, $I_i^{r_1}$, and the deformed label, $L_i^{r_1}$, which is a candidate label for the next slice, I_i,

$$I_i^{r_1} = T_{i-1}^{r_1}(I_{i-1}), \quad (9)$$

$$L_i^{r_1} = T_{i-1}^{r_1}(L_{i-1}^{r_1}), \quad (10)$$

where $L_0^{r_1} = L_0$ is provided by the expert user.

- The same steps are repeated starting from I_n and moving backward to $I_{\lfloor \frac{n}{2} \rfloor + 1}$,

$$T_{j+1}^{r_1} = Reg(I_{j+1}, I_j), \quad (11)$$

where $j \in \{n-1, n-2, \ldots, \lfloor \frac{n}{2} \rfloor + 1\}$. At each step j, the computed registration transformation, T_{j+1}^{r1}, is applied to slice I_{j+1} and its label, L_{j+1}^{r1}, which generates the registered image, $I_j^{r_1}$, and the deformed label, L_j^{r1}, which is a candidate label for the previous slice, I_j,

$$I_j^{r_1} = T_{j+1}^{r_1}(I_{j+1}), \quad (12)$$

$$L_j^{r_1} = T_{j+1}^{r_1}(L_{j+1}^{r_1}), \quad (13)$$

where $L_n^{r_1} = L_n$ is provided by the expert user.

(3) *Image registration direction 2:*

- Starting from $I_{\lfloor \frac{n}{2} \rfloor}$ and moving backward to I_1, each image is registered to the previous image

$$T_{i+1}^{r_2} = Reg(I_{i+1}, I_i), \quad (14)$$

where $i \in \{\lfloor \frac{n}{2} \rfloor - 1, \lfloor \frac{n}{2} \rfloor - 2, \ldots, 1\}$. At each step i, the computed registration transformation, T_{i+1}^{r2}, is applied to slice I_{i+1} and its label, L_{i+1}^{r2}, which generates the registered image, $I_i^{r_2}$ and the deformed

label, L_i^{r2}, which is the candidate label for previous slice, I_i,

$$I_i^{r_2} = T_{i+1}^{r_2}(I_{i+1}), \tag{15}$$

$$L_i^{r_2} = T_{i+1}^{r_2}(L_{i+1}^{r_2}). \tag{16}$$

- The same steps are repeated starting from $I_{\lfloor \frac{n}{2} \rfloor}$ and moving forward to I_{n-1},

$$T_{j-1}^{r_2} = Reg(I_{j-1}, I_j), \tag{17}$$

$$I_j^{r_2} = T_{j-1}^{r_2}(I_{j-1}), \tag{18}$$

$$L_j^{r_2} = T_{j-1}^{r_2}(L_{j-1}^{r_2}), \tag{19}$$

where $j \in \{\lfloor \frac{n}{2} \rfloor + 1, \lfloor \frac{n}{2} \rfloor + 2, \ldots, n-1\}$.

In Eqs. (16) and (19), $L_{\lfloor \frac{n}{2} \rfloor}^{r_2} = L_{\lfloor \frac{n}{2} \rfloor}$ is provided by the expert user.

(4) *Find the best registration for each slice:* Steps 2 and 3 yield two registration results for each slice. In other words, for each slice I_i (I_j) where $i \neq 0$ and $i \neq \lfloor \frac{n}{2} \rfloor$ ($j \neq \lfloor \frac{n}{2} \rfloor$, and $j \neq n$), we have two registered images I_i^{r1} and I_i^{r2} (I_j^{r1} and I_j^{r2}) and two corresponding deformed labels L_i^{r1} and L_i^{r2} (L_j^{r1} and L_j^{r2}). In order to generate the final result, an image similarity measure (i.e., correlation coefficients) is used to calculate the similarity between the registered images from "image registration—direction 1 and 2" and the original images for each slice in the image sequences. These similarity measures are used to combine the two labels as weighted average

$$L_i = \frac{\text{sim}(I_i^{r1}, I_i) \times L_i^{r1} + \text{sim}(I_i^{r2}, I_i) \times L_i^{r2}}{\text{sim}(I_i^{r1}, I_i) + \text{sim}(I_i^{r2}, I_i)}, \tag{20}$$

where in order to obtain a binary result, L_i is binarized with an optimal threshold, which in our experiments was set to 0.25.

For the iBRS algorithm, it is expected that the results will be poor if we only use the first and last slice (instead of the first, middle, and last slice) because only a portion of the prostate is visible in the first and last slices, so the propagation of contours using registration techniques might not work properly as we move toward the middle slice. If we only use the middle slice for segmentation, however, this method works fine for slices close to the middle, although we may lose accuracy as we reach the base or apex slices. This is because the middle slice is usually very different than a slice located five to six slices further along and registration cannot compensate for these differences, which leads to poor results.

5. MATERIALS AND RESULTS

This section presents the test images used in the experiments and the performance evaluation measures. All three registration methods (i.e., rigid, affine, and nonrigid) were used to generate results for MR images with iBRS. For CT images, only the nonrigid registration algorithm was used to generate results.

TABLE I. Description of the prostate MR images used in terms of their dimensions (pixels and mm), slice thickness (mm), and total number of slices per volume dataset where the prostate was visible for segmentation (N).

Total studies	Dimensions (pixels)	Dimensions (mm)	Thickness (mm)	Slices per study
32	256 × 256	100 × 100	3	$10 \leq N \leq 21$
43	256 × 256	120 × 120	3	$9 \leq N \leq 21$
3	256 × 256	140 × 140	4	$7 \leq N \leq 8$
2	512 × 512	140 × 140	3	$10 \leq N \leq 17$
17	512 × 512	150 × 150	2.5–3	$11 \leq N \leq 21$
2	512 × 512	160 × 160	3	$17 \leq N \leq 18$
1	512 × 512	180 × 180	3	14

5.A. Prostate MR images

The MR images used in this study were derived from an online database (http://prostateMRimageDatabase.com). The database contains MR volume datasets provided by Brigham and Women's Hospital, the National Center for Image-guided Therapy, and Harvard Medical School. Images that were originally available in PNG format with the associated text files describing their imaging parameters were converted to DICOM format. The images comprised T2-weighted MR images (T2W-MR) with endorectal coil. The pulse sequence groups in the DICOM headers of most of the T2-weighted images were fast spin echo (FSE), while some were marked as fast relaxation fast spin echo-accelerated (FRFSE-XL). This dataset contained images where the slice thickness ranged from 2.5 to 4.0 mm with varying contrast levels and signal-to-noise characteristics. All of the images were captured with a depth of 16 bits and varied in size from 256 × 256 to 512 × 512 pixels. Complete descriptions of the 100 MRI volume datasets considered in the current study are provided in Table I. The total number of individual slices that contained a portion of prostate was about 1200 images. A radiation oncologist manually contoured all of the MR images for all 100 patients. We used the manual markings, which are also known as the gold standard or ground truth images, to measure the accuracy of our proposed method.

5.B. Prostate MR images for user variability analysis

In addition to the MR images used to analyze the performance of our proposed segmentation algorithm, for the user variability analysis, we used 15 MR image volume datasets (Taken from the same online database as the one used in Sec. 5.A.) which were different from the original data of 100 patients described in Sec. 5.A (with 180 individual slices that contained a portion of prostate). Each volume dataset was manually contoured by five different radiation oncologists.

TABLE II. Description of the prostate MR images used to analyze the user variability in terms of their dimensions (pixels and mm), slice thickness (mm), and total number of slices per volume dataset where the prostate was visible for segmentation (N).

Total studies	Dimensions (pixels)	Dimensions (mm)	Thickness (mm)	Slices per study
11	512 × 512	150 × 150	3	$11 \leq N \leq 17$
1	512 × 512	160 × 160	3	13
3	512 × 512	180 × 180	3	$12 \leq N \leq 22$

Table II shows complete descriptions of the MR images used in the user variability analysis.

5.C. Prostate CT images

We used 17 volume datasets of CT images (with 150 individual slices that contained a portion of prostate) acquired at the London Health Sciences Centre, London, Ontario, Canada, to evaluate the iBRS algorithm using the nonrigid registration method. The image dimensions were 512 × 512 (pixels) and the pixel spacing varied from 0.85 to 1.17 mm. The slice thickness was 3 mm in all volume sets and the total number of slices per study where the prostate was visible for segmentation varied between 8 and 26. An expert manually contoured all of the CT images that contained a portion of the prostate gland for all 17 patient volume datasets (Table III).

5.D. Slice accuracy

The accuracy of individual slices was measured by comparing the automatically generated labels with the ones drawn manually by a clinician (i.e., the ground truth images). Dice similarity coefficient (DSC) (Ref. 33) is a well-known accuracy measure which is defined as

$$\mathrm{DSC} = \frac{2|B_m \bigcap B_a|}{|B_m| + |B_a|}, \tag{21}$$

where B_m and B_a are the manually and automatically generated labels, respectively. $\bigcap$ represents the shared information in the two binary images.

5.E. Estimation of the prostate volume

After the slices of a MR/CT volume dataset have been autosegmented or manually contoured, the area of each slice, $\mathbf{A} = \{A_i, |i \in \{1, \ldots, n\}\}$, is calculated, where n is the number of slices in a volume dataset where a portion of the prostate is visible. The estimated volume of the prostate in each volume dataset or image sequence is then calculated based on A_i and the slice thickness Th, as follows:

$$V = Th \times \left(\frac{A_1 + A_N}{3} + \sum_{i=2}^{N-1} A_i \right). \tag{22}$$

This is similar to the approach used in Ref. 15, although a modification (i.e., adding $\frac{A_1+A_N}{3}$) was made to the equation to consider the start-point and end-point of the prostate volume. In this calculation, it is assumed that the start-point and the end-point of the prostate have a distance of Th from the adjacent slices which means base and apex, respectively. This means that there are two cone-shape volumes with Th as height and A_1 and A_N as bases giving volumes of $Th \times \frac{A_1}{3}$ and $Th \times \frac{A_N}{3}$.

TABLE III. Description of the prostate CT images used in terms of their dimensions (pixels and mm), slice thickness (mm), and total number of slices per volume dataset where the prostate was visible for segmentation (N).

Total studies	Dimensions (pixels)	Dimensions (mm)	Thickness (mm)	Slices per study
7	512 × 512	$447 \times 447 \leq \mathrm{dim} \leq 500 \times 500$	3	$8 \leq N \leq 26$
4	512 × 512	$500 \times 500 \leq \mathrm{dim} \leq 550 \times 550$	3	$8 \leq N \leq 11$
6	512 × 512	$550 \times 550 \leq \mathrm{dim} \leq 600 \times 600$	3	$8 \leq N \leq 18$

5.F. Calculation of the volume accuracy and volume ratio

To calculate the volume accuracy, we use DSC [Eq. (21)] to calculate the Dice value over the entire 3D prostate. We also use another measure, volume ratio, which is the ratio of the volume values of the autosegmentation algorithm results V_a and the manual contouring V_m, respectively,

$$V_{\mathrm{Ratio}}(\%) = \frac{V_a}{V_m} \times 100. \tag{23}$$

5.G. Mean and maximum absolute distances

For each point on the autosegmentation result, we measured the distance from the corresponding point on the manual label to calculate the mean absolute distance (MAD) and maximum absolute distance (MAXD).

5.H. Results for the iBRS algorithm with MR images

We present the results of experiments performed using MR images from 100 patients (a total of 1200 images with labels). Figure 1 shows the prostate MR image sequence (i.e., volume dataset) of one patient where a portion of the prostate gland is visible. As explained in Sec. 4, an expert user manually contours the prostate in the first, middle, and the last slices of a MR image sequence when using the iBRS algorithm. For example, Fig. 1 shows the manual markings (solid white lines) for three slices (i.e., S1, S7, and S12). The solid white rectangles around the segmented prostate represent the ROIs constructed using the prostate boundary defined by the user labels. The dotted rectangles between the segmented slices are the interpolated ROIs for the remaining slices. Figure 2 shows the results of the iBRS autosegmentation algorithm for the example shown in Fig. 1 using three different registration methods. It is clear all three registration methods yielded good results for segmentation of the middle slices in Fig. 1.

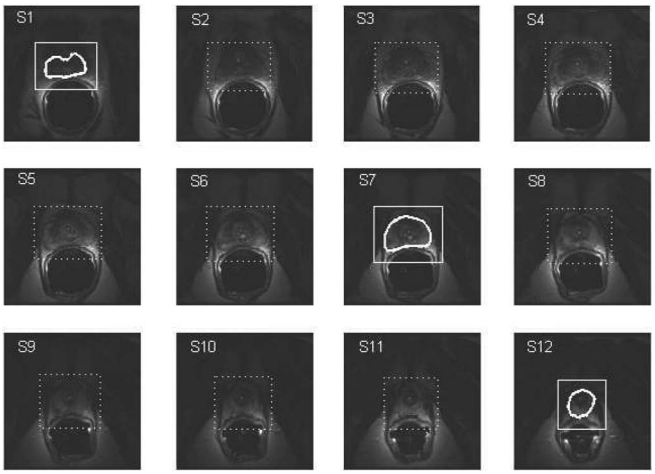

FIG. 1. Prostate MR image sequence for a sample volume dataset. The prostate was marked in the first, middle, and last images by an expert user. The dotted rectangles between the marked images represent the interpolated ROIs calculated using the ROIs of the user labels. The slice numbers are shown in the top left corner. All images have been brightened for display purposes only.

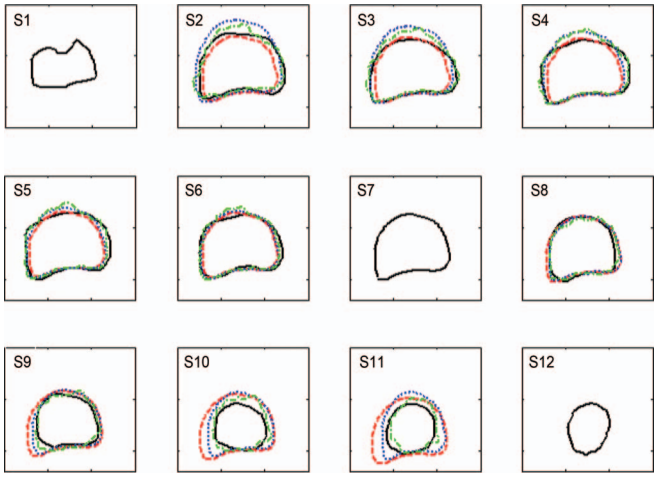

FIG. 2. Autosegmentation results with the iBRS algorithm for the sample volume dataset shown in Fig. 1. The segmentation results are shown for rigid registration (dashed line), affine registration (dotted line), and Demon (nonrigid) registration (dashed-dotted line). The solid line labels are the manual contours provided by an expert user.

Table IV and Fig. 3 summarize the results of autosegmentation of the prostate using the iBRS algorithm for all 100 patients. Almost for all measures, the nonrigid algorithm outperformed the other two methods. The median individual and volume DSCs (In calculating the accuracy, the first, middle, and last slices were excluded to only take the autosegmentation result into account.) increased from 88.51% and 85.53%, respectively, for rigid registration to 91.58% and 89.72%, respectively, for nonrigid registration where the volume ratio decreased from 1.21 for rigid registration to 1.11 for nonrigid registration. MAD value decreased by 0.59 mm for nonrigid registration compared to rigid registration (i.e., 1.94 vs 2.53 mm). Interestingly, MAXD value was slightly higher for nonrigid registration compared to rigid registration (i.e., 6.32 vs 6.25 mm).

The computational time required for the segmentation of one prostate volume dataset, run on a dual core Intel 3.33 GHz processor, is dramatically increased from 13 s (1.17 s per slice) with rigid registration to about 3 min (16.82 s per slice) with nonrigid registration, while affine registration required about 47 s (4.25 s per slice). In time-sensitive settings where it is important to produce the results in a short time, it may be more practical to use rigid registration since it produced reasonably accurate results (e.g., DSC of 88.51%) in a short time (i.e., 13 s).

5.I. Results for the iBRS algorithm using MR images in the user variability analysis

We compared the sensitivity of the iBRS algorithm to the user variability using the 15 volume datasets described in Table II. Each volume dataset was manually contoured by five expert users. Table V presents the results for automated segmentation of the prostates from 15 patients using the iBRS algorithm. The Demon (nonrigid) registration method was used by the iBRS algorithm. The proposed algorithm was robust to user variability, e.g., the standard deviation of the DSC was 1.77%. To calculate the user variability among the experts, STAPLE algorithm[21] was used to create a consensus contour for each slice of the 15 datasets using the five manual segmentations. Next, for each dataset, the manual segmentations of each expert was compared to the corresponding consensus contour using the DSC measure and the results were averaged. This quantified a user agreement of 91.44% which corresponds to a user variability of 8.56%.

5.J. Results with the iBRS algorithm using CT images

We applied the iBRS algorithm with the nonrigid registration method to CT images of the prostate from 17 patients (a total of 150 images) (Table III) and the results were compared with the manually contoured images. The median volume accuracy for all 17 patients was 88.98% ± 3.67% (volume ratio 1.13 ± 0.08). The median DSC for single slices was

TABLE IV. Prostate segmentation median results using the iBRS algorithm for 100 patients, which includes DSC for individual slices (%), DSC for entire volume (%), volume ratio, MAD (mm), MAXD (mm), and processing time (s).

Reg. Alg./accuracy	DSC (Slice) (%)	DSC (Vol.) (%)	Vol. Ratio	MAD (mm)	MAXD (mm)	Time (s)
Rigid registration	88.51 ± 11	85.53 ± 3.09	1.21 ± 0.09	2.53 ± 1.78	6.25 ± 3.61	12.62 ± 7.60
Affine registration	87.16 ± 11	84.44 ± 4.37	1.26 ± 0.12	2.92 ± 2.06	7.06 ± 3.68	47.05 ± 32.15
Demon registration	91.58 ± 7	89.72 ± 2.72	1.11 ± 0.07	1.94 ± 1.13	6.32 ± 3.28	182.04 ± 112.37

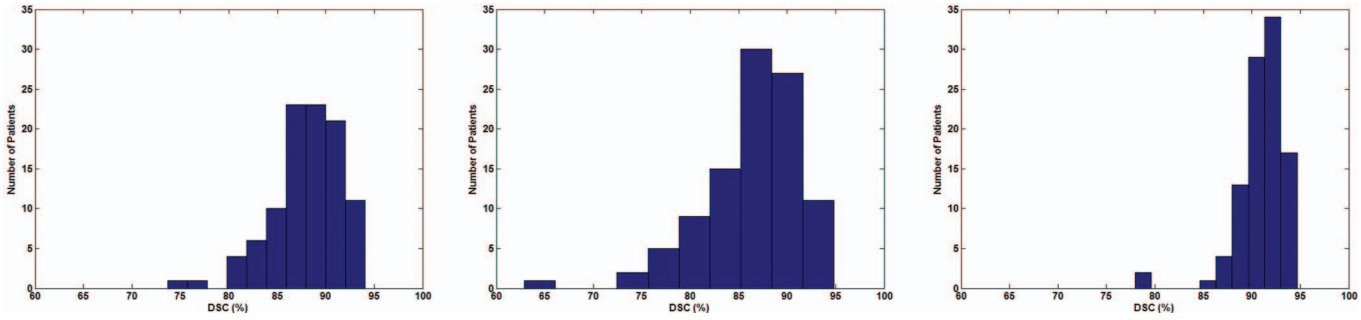

FIG. 3. DSC value comparison between the automatically generated labels and the manual markings for all 100 patients MR images using the iBRS algorithm with three registration methods. (Left) Rigid registration, (Middle) Affine registration, and (Right) Demon (nonrigid) registration.

90.56% ± 4.21%. The average MAD and MAXD values were 2.81 ± 1.09 mm and 8.69 ± 3.23 mm, respectively.

The average prostate segmentation time for a CT volume dataset (run in Matlab prototype) was about 48 s (6 s per slice).

6. DISCUSSION

The contouring of medical images is a major part of diagnosis, active surveillance (e.g., using MR images), and treatment planning (generally using CT scans) but it faces two major challenges. First, manual contouring is a tedious task and requires a significant time commitment by clinicians. Second, there is a considerable amount of uncertainty when determining the boundaries of organs or tumors because of interobserver variability during anatomical contouring.[34] The autosegmentation tools aim to reduce the contouring time (higher efficiency) by generating labels that require less user editing or corrections, and to reduce the amount of interobserver variability (more reliability) by generating base labels so a clinician only needs to edit the automatically generated labels, rather than contouring images completely manually.

The complexity of medical images and the vagueness of the objects of interest in such images mean that most segmentation algorithms require user intervention to correct or edit the autosegmentation results. In the iBRS algorithm, a user is required to contour the first, middle, and last slices of the volume data. The iBRS algorithm registers each image twice. This contrasts with conventional ABS techniques where multiple image registration may be required, depending on the size of the atlas and the algorithm design. More frequent use of image registrations incurs higher computational costs, which is a major factor that significantly limits the scalability of ABS.

In terms of the overall accuracy in MR images, the rigid registration performed slightly better compared to affine registration. This may be due to the selected metric as similarity measure in the implementation (i.e., sum of squared distances). However, the nonrigid registration boosted the accuracy in almost all measures (e.g., DSC of 91.58%). This was expected because nonrigid registration usually works better for soft tissues, such as the prostate, which are deformable. The highly accurate results are interesting given the fact that no atlas was used. This is due to exploiting the interslice redundancy among slices in a volume dataset. The consequent slices usually share highly redundant information so propagating the registration result from one slice (e.g., the middle slice) through the other slices (e.g., slices from the middle toward the first) yields high accuracy results. For all three registration techniques, the accuracy of slices near the base/apex were lower than the mid slices if only a small portion of the prostate was visible. Figure 4 illustrates this by measuring the DSC of slices with respect to the distance of the slice from the midslice. It was also observed that the slice thickness of the image volumes affects the accuracy of results; the smaller the slice thickness, the higher the accuracy of results. For our MRI datasets of 100 patients, the slice thicknesses are 2.5 mm (4 patients) 3 mm (93 patients), and 4 mm (3 patients) with the median DSCs of 91.04%, 89.73%, and 88.45%, respectively.

TABLE V. Prostate segmentation median results using the iBRS algorithm (with Demon registration) for 15 patients for user variability analysis, which includes DSC for individual slices (%), DSC for entire volume (%), volume ratio, MAD (mm) and MAXD (mm).

Experts/ accuracy	DSC (slice) (%)	DSC (volume) (%)	Volume ratio	MAD (mm)	MAXD (mm)
1	90.74	90.22	1.08	1.79	5.34
2	92.14	89.74	1.10	1.71	5.59
3	87.32	86.35	1.16	2.66	7.51
4	90.29	88.61	1.14	2.05	6.55
5	89.66	87.57	1.18	2.70	7.45
Mean ±STD	90.03 ± 1.77	88.50 ± 1.58	1.13 ± 0.04	2.18 ± 0.47	6.49 ± 1.01

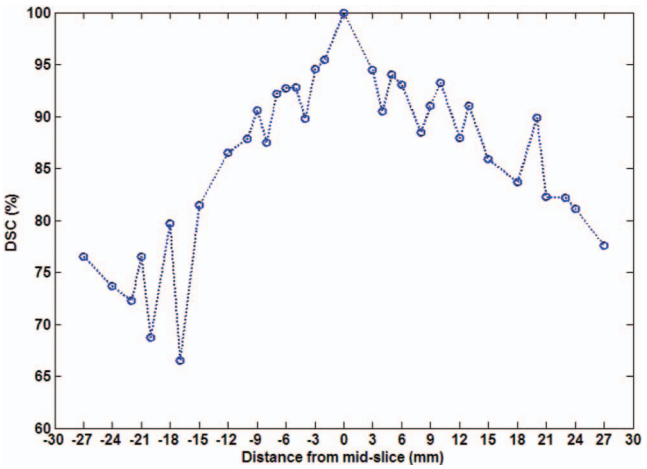

FIG. 4. Average DSC values for slices with respect to their distance from the midslice in prostate volume.

The iBRS algorithm also produced highly accurate results for CT images using the nonrigid registration algorithm (i.e., median volume accuracy and individual slice accuracy of 88.98% and 90.56%, respectively).

In terms of the computational costs, the iBRS algorithm required 1.17 s per slice for rigid and 17 s per slice for nonrigid registration. Even with the rigid registration, the accuracy of the proposed algorithm with MR images were almost identical to the best result reported in the previous studies (i.e., DSC of 88.51% versus up to 88%, Sec. 2) while the processing time was much shorter (i.e., 1.17 s per slice or 13 s per volume). The iBRS algorithm was implemented as a prototype in Matlab but the measured time was still in the order of seconds, whereas the computational times reported in previous studies in the literature were several minutes, even though most of them were implemented in C++. This was because our algorithm only used two registrations per image and no pre- or postprocessing.

The proposed algorithm was evaluated to determine the effect of the user variability on the segmentation results using the datasets of 15 patients, which were contoured by five different radiation oncologists. It was confirmed that the algorithm was insensitive to user variability where the average DSC variation was 1.77%.

The results reported for MR images in this paper were for more than 100 patients volume datasets (about 1200 slices). The large dataset used in our experiments ensured the reliability of the results reported. The results for the iBRS algorithm with CT images confirmed the applicability of our proposed interslice registration-based algorithm for prostate segmentation in both MR and CT modalities.

Since even rigid registration of adjacent slices already gives good performance, one might naturally expect that a simple interpolation method should give a reasonable results where the first, middle, and last slices manual labels are used to interpolate the contours of the remaining slices. We tested this hypothesis on all 100 patients MR data and it was found that with simple linear interpolation, the median DSC value is 82.59%, which is significantly below what our algorithm yields (i.e., 91.58%).

In addition to prostate volume estimation for PSA density calculation, the proposed method in this paper is well suited for treatment planning for radiation therapy where 2D images and contours are used for delineation of regions of interest. As a future work, the 2D contours created by the iBRS algorithm can be used to reconstruct the 3D surface of the prostate gland. There are surface reconstruction methods proposed in the literature that can be applied to the result of the iBRS algorithm. For example, Treece *et al.*[35] proposed a surface reconstruction method using the 2D contours based on maximal disc guided interpolation. In another work, Kazhdan *et al.*[36] showed that the surface reconstruction problem for a set of oriented points on 2D contours can be solved using Poisson problem. This method was used in Ref. 37 to reconstruct the 3D surface of breast MRI from 2D contours.

7. CONCLUSION

In this paper, we introduced a new algorithm for segmenting the prostate gland in T2-weighted MR and CT images. The *Inter-Slice Bidirectional Registration-based Segmentation* or iBRS algorithm requires the input of labels for three slices (first, middle, and last) in a volume dataset, before it automatically generates the labels of the remaining slices. The proposed algorithm exploits the interslice data redundancy of the images in a volume dataset and eliminates the need for an atlas, which minimizes the computational costs. We verified the performance of the algorithm using a large dataset of prostate MR images (1200 images of 100 patient volume datasets), which demonstrated its high accuracy depending on the registration method used (87%–92% DSC for individual slices and 84%–90% for volume). The iBRS algorithm was also evaluated to determine the user variability effect on the segmentation results using datasets from 15 patients, which were contoured by five clinicians. It was confirmed that the algorithm was robust to user variability and the DSC variation was only 1.77% among different users. The iBRS algorithm was also applied to prostate CT images from 17 patients where the average accuracies for the volume and individual slices were 89% and 91% (DSC), respectively. The computational time required by the algorithm varied from 1.17 s to 17 s per segmentation in MR images (6 s in CT images). The computational time was measured using Matlab prototypes of the algorithm. It is expected that C++ implementations of the algorithm will reduce the processing time significantly.

ACKNOWLEDGMENTS

The authors would like to thank FedDev Ontario, Canada, for supporting this research. The authors would also like to thank Segasist Technologies for providing DICOM datasets and assistance for implementing and running the experiments.

[a]Electronic mail: farzad.khalvati@uwaterloo.ca

[1]Prostate Cancer Canada, "What's your number? Prostate Cancer Canada Annual Report," 2010 (available URL: www.prostatecancer.ca).
[2]M. Roach, P. Faillace-Akazawa, C. Malfatti, J. Holland, and H. Hricak, "Prostate volumes defined by magnetic resonance imaging and

computerized tomographic scans for three-dimensional conformal radiotherapy," Int. J. Radiat. Oncol., Biol., Phys. **35**, 1011–1018 (1996).
[3]K. Kagawa, W. R. Lee, T. E. Schultheiss, M. A. Hunt, A. H. Shaer, and G. E. Hanks, "Initial clinical assessment of CT-MRI image fusion software in localization of the prostate for 3D conformal radiation therapy," Int. J. Radiat. Oncol., Biol., Phys. **38**, 319–325 (1997).
[4]R. J. Steenbakkers, K. E. Deurloo, P. J. Nowak, J. V. Lebesque, M. van Herk, and C. R. Rasch, "Reduction of dose delivered to the rectum and bulb of the penis using MRI delineation for radiotherapy of the prostate," Int. J. Radiat. Oncol., Biol., Phys. **57**, 1269–1279 (2003).
[5]J. H. Jonsson, M. G. Karlsson, M. Karlsson, and T. Nyholm, "Treatment planning using MRI data: An analysis of the dose calculation accuracy for different treatment regions," Radiat Oncol. **5**(62), (2010).
[6]C. H. Bangma, A. Q. Niemer, D. E. Grobbee, and F. H. Schrder, "Transrectal ultrasonic volumetry of the prostate: In vivo comparison of different methods," Prostate **28**, 107–110 (1996).
[7]S. Hoffelt, L. Marshal, M. Garzotto, A. Hung, J. Holland, and T. M. Beer, "A comparison of CT scan to transrectal ultrasound measured prostate volume in untreated prostate cancer," Int. J. Radiat. Oncol., Biol., Phys. **57**, 29–32 (2003).
[8]L. M. Eri, H. Thomassen, B. Brennhovd, and L. L. Haheim, "Accuracy and repeatability of prostate volume measurements by transrectal ultrasound," Prostate Cancer Prostatic Dis **5**, 273–278 (2002).
[9]B. van Ginneken, A. F. Frangi, J. J. Staal, B. M. ter Haar Romeny, and M. A. Viergever, "Active shape model segmentation with optimal features," IEEE Trans. Med. Imaging **21**, 924–933 (2002).
[10]T. Cootes, C. Taylor, D. Cooper, and J. Graham, "Active shape models-their training and application," Comput. Vis. Image Underst. **61**, 38–59 (1995).
[11]H. M. Ladak, F. Mao, Y. Wang, D. B. Downey, D. A. Steinman, and A. Fenster, "Prostate boundary segmentation from 2D ultrasound images," Med. Phys. **27**, 1777–1788 (2000).
[12]D. Shen, Y. Zhan, and C. Davatzikos, "Segmentation of prostate boundaries from ultrasound images using statistical shape model," IEEE Trans. Med. Imaging **22**, 539–551 (2003).
[13]A. C. Hodge, A. Fenster, D. B. Downey, and H. M. Ladak, "Prostate boundary segmentation from ultrasound images using 2D active shape models: Optimisation and extension to 3D," Comput. Methods Programs Biomed. **84**, 99–113 (2006).
[14]Y. Zhan and D. Shen, "Deformable segmentation of 3-D ultrasound prostate images using statistical texture matching method," IEEE Trans. Med. Imaging **25**, 256–272 (2006).
[15]R. Toth, B. N. Bloch, E. M. Genega, N. M. Rofsky, R. E. Lenkinski, M. A. Rosen, A. Kalyanpur, S. Pungavkar, and A. Madabhushi, "Accurate prostate volume estimation using multifeature active shape models on T2-weighted MRI," Acad. Radiol. **18**, 745–754 (2011).
[16]S. Martin, J. Troccaz, and V. Daanen, "Automated segmentation of the prostate in 3D MR images using a probabilistic atlas and a spatially constrained deformable model," Med. Phys. **37**, 1579–1590 (2010).
[17]S. Klein, U. A. van der Heide, I. M. Lips, M. van Vulpen, M. Staring, and J. P. W. Pluim, "Automatic segmentation of the prostate in 3D MR images by atlas matching using localized mutual information," Med. Phys. **35**, 1407–1417 (2008).
[18]S. Klein, U. A. van der Heide, B. W. Raaymakers, A. N. T. J. Kotte, M. Staring, and J. P. W. Pluim, "Segmentation of the prostate in MR images by atlas matching," in *Proceedings of the IEEE Conference on Biomedical Imaging* (2007), pp. 1300–1303.
[19]J. Dowling, J. Fripp, P. Greer, J. Patterson, S. Ourselin, and O. Salvado, *Proceedings of 2009 MICCAI Prostate Segmentation Challange* (London, 2009), pp. 17–24.
[20]T. R. Langerak, U. A. van der Heide, A. N. T. J. Kotte, M. A. Viergever, M. van Vulpen, and J. P. W. Pluim, "Label fusion in atlas-based segmentation using a selective and iterative method for performance level estimation (SIMPLE)," IEEE Trans. Med. Imaging **29**, 2000–2008 (2010).
[21]S. K. Warfield, K. H. Zou, and W. M. Wells, "Simultaneous truth and performance level estimation (STAPLE): An algorithm for the validation of image segmentation," IEEE Trans. Med. Imaging **23**, 903–921 (2004).
[22]S. S. Mahdavi, N. Chng, I. Spadinger, W. J. Morris, and S. E. Salcudean, "Semi-automatic segmentation for prostate interventions," Med. Image Anal. **15**, 226–237 (2011).
[23]W. Qiu, J. Yuan, E. Ukwatta, D. Tessier, and A. Fenster, "Three-dimensional prostate segmentation using level set with shape constraint based on rotational slices for 3D end-firing TRUS guided biopsy," Med. Phys. **40**, 072903 (12pp.) (2013).
[24]J. B. A. Maintz and M. A. Viergever, "A survey of medical image registration," Med. Image Anal. **2**, 1–36 (1998).
[25]L. G. Brown, "A survey of image registration techniques," ACM Comput. Surv. **24**, 325–376 (1992).
[26]D. J. Kroon, "Multimodality non-rigid demon algorithm image registration," MatlabCentral, 2008 (available URL: www.mathworks.com/matlabcentral/fileexchange/21451-multimodality-non-rigid-demon-algorithm-image-registration).
[27]J. P. Thirion, "Image matching as a diffusion process: An analogy with Maxwell's demons," Med. Image Anal. **2**(3), 243–260 (1998).
[28]H. Wang, L. Dong, J. O'Daniel, R. Mohan, A. S. Garden, K. K. Ang, D. A. Kuban, M. Bonnen, J. Y. Chang, and R. Cheung, "Validation of an accelerated 'demons' algorithm for deformable image registration in radiation therapy," Phys. Med. Biol. **50**(12), 2887–2905 (2005).
[29]A. Guimond, A. Roche, N. Ayache, and J. Meunier, "Three-dimensional multimodal brain warping using the demons algorithm and adaptive intensity corrections," IEEE Trans. Med. Imaging **20**(1), 58–69 (2001).
[30]D. J. Kroon and C. H. Slump, "MRI modality transformation in demon registration," in *Proceedings of the IEEE International Symposium on Biomedical Imaging: From Nano to Macro, ISBI 09* (2009), pp. 963–966.
[31]D. L. Langer, T. H. van der Kwast, A. J. Evans, J. Trachtenberg, B. C. Wilson, and M. A. Haider, "Prostate cancer detection with multi-parametric MRI: Logistic regression analysis of quantitative T2, diffusion-weighted imaging, and dynamic contrast-enhanced MRI," Magn. Reson. Imaging **30**, 327–334 (2009).
[32]B. Hentschel, W. Oehler, D. Strau, A. Ulrich, and A. Malich, "Definition of the CTV prostate in CT and MRI by using CT-MRI image fusion in IMRT planning for prostate cancer," Strahlenther. Onkol. **187**(3), 183–190 (2011).
[33]L. R. Dice, "Measure of the amount of the ecologic association between species," Ecology. **26**, 297–302 (1945).
[34]M. G. Jameson, L. C. Holloway, and P. J. Vial, "A review of methods of analysis in contouring studies for radiation oncology," J. Med. Imaging Radiat. Oncol. **54**, 401–410 (2010).
[35]G. M. Treece, R. W. Prager, A. H. Gee, and L. Berman, "Surface interpolation from sparse cross sections using region correspondence," IEEE Trans. Med. Imaging **19**, 1106–1114 (2000).
[36]M. Kazhdan, M. Bolitho, and H. Hoppe, "Poisson surface reconstruction," in *Proceedings of the Fourth Eurographics Symposium on Geometry Processing, SGP 06* (Eurographics Association, Aire-la-Ville, Switzerland, 2006), pp. 61–70.
[37]C. Gallego Ortiz and A. L. Martel, "Automatic atlas-based segmentation of the breast in MRI for 3D breast volume computation," Med. Phys. **39**(10), 5835–5848 (2012).